

## Study of the Kinetics, Thermodynamics, and Adsorption Isotherm of Diamine Green B Dye Using the Biocatalyst Laccase@Fe-BTC

F. Tahmasebi<sup>1</sup>, R. Alizadeh<sup>2,3\*</sup>, N. Samadi<sup>1</sup>

<sup>1</sup> Department of Analytical Chemistry, Faculty of Chemistry, Urmia University, P.O. Box: 1138, Urmia, Iran.

<sup>2</sup> Department of Civil Engineering, Faculty of Engineering, Qom university of Technology, P.O. Box: 1519-37195, Qom, Iran.

<sup>3</sup> Department of Chemical, Materials & Polymer Engineering, Buein Zahra Technical University. P.O. Box: 3451745346, Buein zahra, Qazvin.

### ARTICLE INFO

#### Article history:

Received: 27 Feb 2025

Final Revised: 18 May 2025

Accepted: 21 May 2025

Available online:

#### Keywords:

Diamine Green B Adsorption

Fe-BTC

Dye removal

Laccase enzyme

Kinetics thermodynamic

Isotherm

### ABSTRACT

*In this study, the isotherm, kinetic, and thermodynamic properties of diamine green B dye adsorption were investigated using enzymatic metal-organic frameworks. First- and second-order kinetic models, along with the Elovich kinetic model, as well as Langmuir and Freundlich isotherm models, were applied to evaluate the data. Based on previous studies, the dye adsorption efficiency of this material was assessed by examining the effects of contact time, adsorbent dosage, and initial dye concentration. The optimal adsorption conditions for this nano-adsorbent were determined to be a contact time of 45 min and an adsorbent dosage of 5 g/L. The calculated thermodynamic parameters ( $\Delta G$ ,  $\Delta H$ , and  $\Delta S$ ) indicate that the adsorption of the dye onto the enzymatic organometallic adsorbent is spontaneous, endothermic, and associated with an increase in randomness. The process followed the Elovich kinetic model. Among the tested isotherm models, the Freundlich isotherm provided the best fit to the experimental data. Prog Color Colorants Coat. 19 (2026), 507-517© Institute for Color Science and Technology.*

### 1. Introduction

Metal-organic frameworks (MOFs) are bi- or three-dimensional nanoporous materials, generally crystalline, formed by metal ions or metal clusters connected through multidentate organic ligands. One of the most recent applications of MOFs involves the immobilization of enzymes. Moreover, the hybrid organic-inorganic nature of certain MOFs appears to promote interactions with enzymes, as solid active biocatalysts can form simply by bringing the two components into contact, even when the material lacks sufficiently large pores to accommodate the enzyme [1].

The aromatic components in dye structures increase their toxicity and prevent biodegradability. Diamine green B, with the molecular formula  $C_{34}H_{22}N_8Na_2O_{10}S_2$ ,

is an anionic azo dye commonly used for dyeing fibers. Surface adsorption is one method used for removing such dyes. Nanostructured adsorbents, due to their high surface-to-volume ratio, offer greater adsorption capacity compared to conventional adsorbents. Their higher porosity further contributes to this increased capacity [2].

Additionally, nanostructured adsorbents generate less waste, which can be more easily collected. In addition, the reusability of the adsorbent supports the economic viability of this process. Among mesoporous silica adsorbents, the MCM and SBA families of molecular sieves have attracted attention due to their high surface area, high porosity, uniform pore size distribution, and tunable surface characteristics.

\*Corresponding author: \* alizadeh\_environment@yahoo.com  
<https://doi.org/10.30509/pccc.2025.167477.1366>

To expand the range of applications, modifications can be made within the channel walls or by attaching functional groups to the surface of these materials. New structures have also been developed using nonionic surfactants in acidic media. One of the most recent applications of MOFs involves the immobilization of enzymes. Enzymes are proteins that facilitate chemical reactions in living organisms through catalysis. They are widely used across various industries due to their high specificity, catalytic efficiency, and environmental compatibility. Enzymatic immobilization techniques are used to protect enzymes and improve their stability. Laccase enzymes can be readily obtained from various sources and are widely used in biotechnological processes due to their ability to catalyze oxidation reactions using only atmospheric oxygen as the electron acceptor. Unlike other oxidases that require cofactors, this property makes laccases particularly suitable for applications in bioremediation, biosensing, and several other processes that will be discussed further [3].

A variety of materials and nanomaterials can be used for enzyme immobilization, including natural polymers such as collagen, alginate, chitosan, and cellulose, as well as inorganic materials like zeolites, ceramics, silica, charcoal, and glass. Enzymes can be immobilized onto these carriers through adsorption, covalent bonding, pore entrapment, encapsulation, crosslinking, or ligand affinity. Several techniques are available to synthesize or prepare these materials for enzyme anchoring, including electrospinning, matrix-assisted pulsed laser evaporation (MAPLE), soft plasma polymerization, 3D and laser printing, and the use of crosslinked enzyme aggregates, nanoflowers, and MOFs [4].

MOF materials with pore sizes in the mesoporous range (diameters greater than 2.0 nm) can encapsulate certain small enzymes. In addition, the hybrid organic–inorganic nature of some MOFs appears to promote interactions with enzymes, allowing the formation of solid, active biocatalysts simply by bringing the two components into contact, even when the material lacks sufficiently large pores to accommodate the enzyme fully. Laccase is a multicopper oxidoreductase enzyme that can oxidize various organic compounds, including dyes. Laccases tend to be unstable at room temperature, and their conformation often changes in strongly acidic or alkaline environments, reducing their effectiveness. Rationally linking enzymes to suitable supports can significantly improve the stability and reusability of

native enzymes. However, during the immobilization process, several factors may lead to a reduction in enzymatic activity. Therefore, selecting an appropriate support is essential to maintain the activity and cost-effectiveness of immobilized catalysts. MOFs are porous and structurally straightforward hybrid support materials. Additionally, the coordination properties of the metal–ligand framework in MOFs may produce a synergistic effect with the metal ions at the active sites of metalloenzymes, thereby improving their catalytic activity [5, 6].

In this study, laccase enzyme was coated onto a metal-organic nanostructured adsorbent. In these cubic nanoparticles, half of the octahedral sites and one-eighth of the tetrahedral sites are occupied by trivalent iron ions. The addition of laccase to these nanoparticles yields cluster-shaped materials capable of removing dyes from industrial wastewater. Nanostructured materials with magnetic and electrical properties are converted into magnetically coated materials. Surface-supported metal-organic frameworks (SMOFs), also known as porous coordination polymers, have drawn increasing interest from researchers in recent years [7]. These structures represent a new class of porous materials formed by connecting metal ions or clusters to polydentate allylic ligands through covalent bonds. Compared to other porous materials such as zeolites, silica, and activated carbon, coordination polymers have been proposed as versatile materials due to their tunable pore surface, size, shape, and functional groups. Magnetic metal–organic nanocomposites possess the ability to adsorb and degrade dyes in photodegradation processes, even in the absence of light. In this study, a low-cost enzyme was used in the sequential removal of Diamine Green B dye. This capability is attributed to the easy separation of metal–organic materials under a magnetic field, which significantly reduces operational costs. Laccase catalyzes the single-electron oxidation of compounds using molecular oxygen as the electron acceptor, generating active radicals that degrade dye molecules [6-8].

## 2. Experimental

### 2.1. Materials

The materials used in this study included laccase enzyme derived from *Aspergillus niger*, Diamine green B dye, benzene tricarboxylic acid ( $H_3BTC$ ), the solvent *N,N*-dimethylformamide, ethanol, methanol, iron(III)

nitrate nonahydrate ( $\text{Fe}(\text{NO}_3)_3 \cdot 9\text{H}_2\text{O}$ ), nitric acid, sodium hydroxide, and hydrochloric acid. All chemicals were purchased from Sigma-Aldrich, Finland. Enzyme-enhanced metal-organic nanoadsorbents, prepared using modified laccase enzyme and previously characterized by Scanning electron microscope (SEM) and X-ray techniques, were employed in earlier work by this group [1].

## 2.2. Methods

### 2.2.1. Synthesis of Laccase@Fe-BTC powder

Fe-BTC powder was synthesized via a solvothermal process using chemical precursors in an autoclave system. Initially,  $\text{H}_3\text{BTC}$  and  $\text{Fe}(\text{NO}_3)_3 \cdot 9\text{H}_2\text{O}$  were dissolved separately in DMF and then mixed to form a homogeneous solution. The mixture was sonicated and subsequently heated at  $110\text{ }^\circ\text{C}$  for 6 h to promote the formation of MOF carriers. After synthesis, the obtained Fe-BTC particles were collected, washed, and dried to yield uniform MOF carriers with controlled morphology.

Subsequently, the prepared Fe-BTC carriers were used as supports for enzyme immobilization. Laccase was immobilized onto the surface of Fe-BTC by incubating 7 g of the dried material in a phosphate buffer solution containing 1 ppm laccase for 48 h in a hot water bath, leading to the formation of biocatalyst particles (Lc@Fe-BTC), as illustrated in Figure 1.

To prepare and analyze the samples, a spectro-

photometer and a Philips X-ray diffractometer ( $\lambda = 1.54056\text{ \AA}$ , 40 kV, 35 mA) were used to determine the crystallinity and structural composition of the synthesized material. IR spectra were recorded using a Bruker Vertex 70 spectrometer (Germany) over a wave-number range of  $4000\text{--}400\text{ cm}^{-1}$ . Morphological analysis was performed using a field emission scanning electron microscope (FESEM). Brunauer-Emmett-Teller (BET) analysis for specific surface area, functional groups, pore size distribution, and specific pore volume of the prepared samples was carried out using a TriStar II 3020 instrument (Micromeritics, USA).

### 2.2.2. Adsorption experiments

Decolorization efficiency and the amount of dye adsorbed onto the MOF adsorbent (in mg/g, referred to as adsorption capacity) were calculated using equations 1 and 2, respectively. In this study, key parameters affecting the adsorption process, including dye concentration, adsorbent dosage, and contact time, were investigated using an experimental design approach. In these equations,  $C_0$  is the initial dye concentration (mg/L),  $C_e$  is the equilibrium concentration (mg/L),  $q_e$  is the adsorption capacity (mg/g),  $M$  is the mass of adsorbent (g), and  $V$  is the volume of the solution (L).

$$R(\%) = \frac{(C_0 - C_e) \times 100}{C_0} \quad (1)$$

$$(q_e) = \frac{(C_0 - C_e)}{M} \quad (2)$$

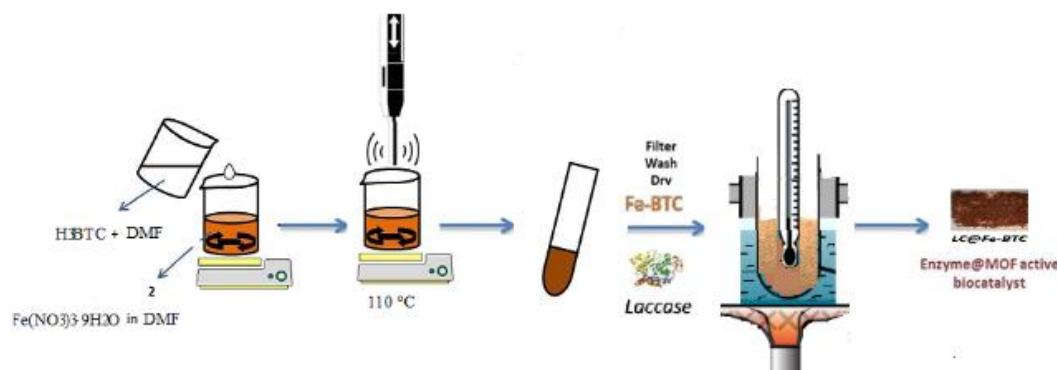


Figure 1: Schematic illustration of the preparation of Lc@Fe-BTC.

### 3. Results and Discussion

#### 3.1. Adsorbent Characterization

X-ray diffraction (XRD) was used to assess the qualitative properties, including crystal orientation, the presence of sharp peaks, purity, crystallinity, and the single-phase nature of the material. Using the intensity and average peak width, the crystallite size was calculated using the Scherrer equation. In equation 3,  $L$  is the average crystallite size,  $K$  is the Scherrer constant (0.9),  $\lambda$  is the X-ray wavelength (1.54060 Å),  $\theta$  is the diffraction angle of each peak, and  $\beta$  is the full width at half maximum (FWHM) of the peak in radians. Comparison between the XRD patterns of enzyme-containing and enzyme-free nanosorbents shows a significant difference in peak intensity, for example, in the sample containing LC, although the peaks are relatively similar to those without LC, the peaks have a much higher intensity, and this is exactly consistent with comparisons with other sources in this field (Figures 3 and 4). The average crystallite size  $L$ , calculated using the Debye-Scherrer equation (equation 3), was 52.8 nm [9, 10].

$$L = K \lambda / \beta \cos \theta \quad (3)$$

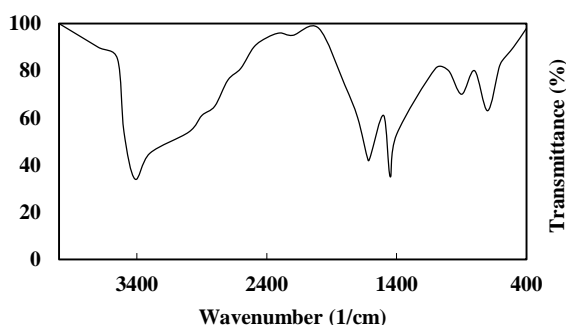


Figure 2: FTIR of the Fe-BTC sample.

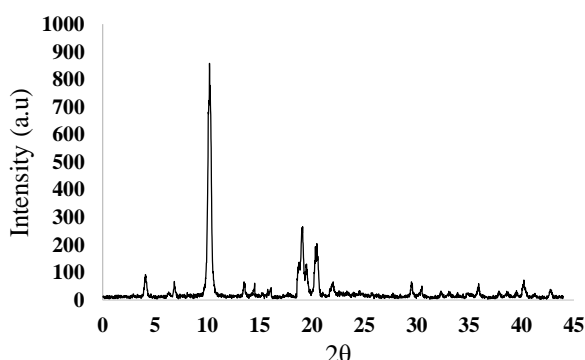


Figure 3: XRD of the LC @Fe-BTC sample.

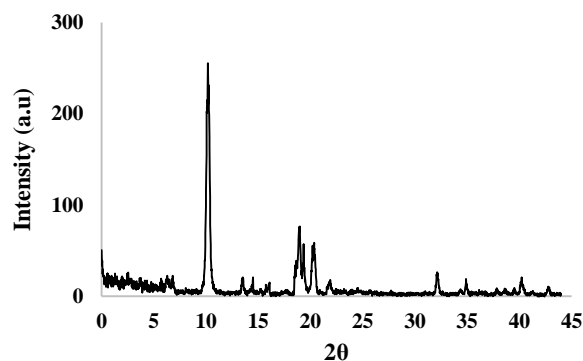


Figure 4: XRD of the Fe-BTC sample.

Scanning electron microscopy (SEM) images provide valuable insight into the morphology and structural organization of the synthesized Fe-BTC and Lc@Fe-BTC materials. As shown in Figure 5, Fe-BTC exhibits a heterogeneous morphology composed of densely packed clusters and agglomerates of irregular nanoparticles that fuse into porous secondary structures with rough surfaces and abundant interparticle voids. The nanoscale size of the primary particles contributes to a high surface area and interconnected channels, features that are advantageous for adsorption processes and typical of Fe-BTC formed via solvothermal synthesis. In Figure 6, the Lc@Fe-BTC sample shows clear morphological changes after enzyme immobilization: while the clustered architecture is preserved, the surface appears more compact and slightly smoother due to the coating of laccase, which partially fills surface cavities and intergranular spaces and creates a more cohesive structure. Comparison of the two images indicates that the immobilization process does not disrupt the framework; instead, the uniform distribution and repetitive geometric organization remain intact, confirming structural stability and successful functionalization. The observed nanoparticle aggregation and resulting mesoporous voids enhance mass transfer and facilitate dye diffusion toward active sites, while the rough porous texture increases the number of accessible binding sites [11]. Overall, SEM analysis confirms successful Fe-BTC nanostructure synthesis and demonstrates that laccase immobilization modifies surface characteristics without compromising the hierarchical porous architecture required for efficient adsorption and biocatalytic performance. According to the particle size distribution obtained by the dynamic light scattering (DLS) method, these particles have an average diameter of 30–36 nm (Figure 7).

### 3.2. Response Surface Statistical Method

The analysis was conducted using the response surface methodology (RSM) with a central composite design, involving three variables at three levels [12]. The variables included dye concentration, contact time, and the amount of enzymatic adsorbent (Table 2).

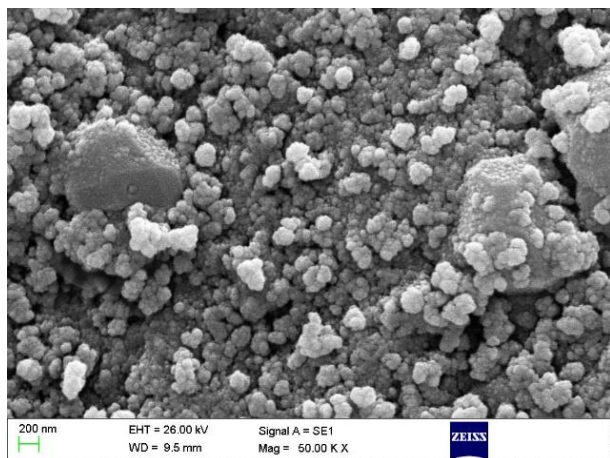


Figure 5: SEM image of Fe-BTC.

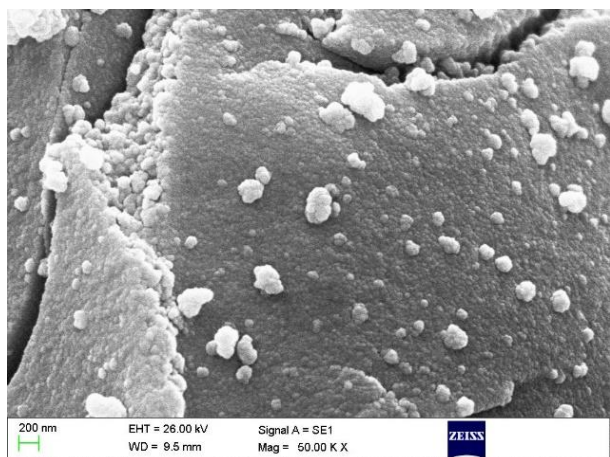


Figure 6: SEM image of LC@Fe-BTC.

Table 1: Immobilization efficiency and catalytic performance of in-situ biocatalysts Lc@Fe-BTC-x, where x refers to the synthesis preparation time.

Biocatalyst Enzyme	Enzyme immobilized/%
Lac@Fe-BTC-1 h	98
Lac@Fe-BTC-1 h	99
Lac@Fe-BTC-4 h	100
Lac@Fe-BTC-22 h	100

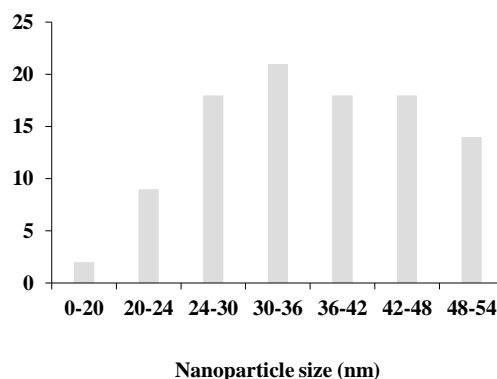


Figure 7: Particle size intensity distribution of the Fe-BTC sample obtained by the DLS method, showing an average particle size of 30–36 nm based on intensity.

Table 2: Range of variables used in the central composite design (CCD) method.

Variable	Symbol	Low	Medium	High
		-1	0	1
Time (Minutes)	A	5	32.5	60
Dye concentration (mg/l)	B	90.7	397.15	611.39
Adsorbent (g/l)	C	1	3	5

#### 3.2.1. Modeling dye removal using an enzymatically functionalized adsorbent via multivariate linear regression

Multivariate linear regression (MLR) was used to model the adsorption of the target dye [13]. The design variables were calculated using a quadratic regression equation (equation 4), where  $B_i$  represents the linear coefficient,  $B_{ii}$  the squared coefficient, and  $B_{ij}$  the interaction coefficient (all of which are fitting constants).  $X_i$ ,  $X_i^2$ , and  $X_i X_j$  denote the independent variables,  $B_0$  is the intercept, and  $Y$  is the response. Based on the values predicted by the model, 15 experiments were conducted for each factor [14, 15].

$$Y = B_0 + \sum B_i \cdot X_i + \sum B_{ii} \cdot X_i^2 + \sum \sum B_{ij} \cdot X_i \cdot X_j \quad (4)$$

The number of test points was determined using equation 5, where  $K$  represents the number of variables and  $C_0$  denotes the number of centre points. In this study, both  $K$  and  $C_0$  were set to 3.

$$N=2K(K-1)+C0 \quad (5)$$

Based on the values determined by the model, 15 experiments were conducted for each factor, with their characteristics presented in Table 3.

The selected software was used to design the experiments. The resulting model is represented by equation 4. Diagrams illustrating the effects of primary factors, factor interactions, and the response surface were generated based on the analysis of variance (ANOVA) table. Design-Expert software was employed for modeling using the MLR method [16-18].

The equation obtained from fitting the response surface for the response parameter  $R$  is presented as equation 6.

$$\%R=87.61+10.32A-3.99B+18.32C-0.61AB-0.90AC+5.33BC-6.51A^2-1.84B^2-9.22C^2 \quad (6)$$

A statistical evaluation of equation 6 was conducted using the F-test, which measures the deviation of the data from the mean, along with ANOVA for the quadratic response surface model. The ANOVA results confirm the model's validity. The F-value of 73 is relatively high, indicating that the model provides a good fit for the experimental data. Additionally, the  $p$ -value is less than 0.05, confirming the statistical significance of the model. In this model, the parameters  $BC$ ,  $C^2$ ,  $A^2$ ,  $C$ ,  $B$ , and  $A$  were identified as significant factors. The equation obtained from fitting the response surface for the parameter  $q$  is presented as equation 7.

$$q=101.63+16.48A+65.67B-50.71C+10.23AB-15.44AC-23.94BC-3.80A^2-13.44B^2+23.17C^2 \quad (7)$$

In this model, the  $p$ -value is less than 0.0001 and the F-value is 56.45, indicating strong statistical significance. The parameters  $C^2$ ,  $BC$ ,  $AC$ ,  $C$ , and  $B$  were identified as influential factors. Statistical evaluation of Equation (7) was performed using the F-test and ANOVA for the quadratic response surface model, with the results presented in Table 4. The ANOVA data confirm the accuracy of the quadratic model. The F-value reflects the deviation of the data from the mean [19, 20]. For a model that accurately predicts experimental results, a high F-value and a  $p$ -value less than 0.05 indicate statistical significance. The adjusted  $R^2$  ( $R^2_{adj}$ ) and predicted  $R^2$  ( $R^2_{pred}$ ) values are 0.9786 and 0.9333, respectively,

demonstrating strong agreement and indicating that the model provides a reliable fit to the experimental data.

**Table 3:** Characteristics of the dye solution and other components used in the experiments.

N	Time (min) A	Dye (mg/l) B	Adsorbent (g/l) C
1	5	300	5
2	5	399	1
3	5	100	3
4	60	300	1
5	5	500	3
6	32.5	500	1
7	60	500	3
8	32.5	100	5
9	32.5	300	3
10	60	100	3
11	32.5	300	3
12	32.5	500	5
13	60	300	5
14	32.5	300	3
15	32.5	100	1

**Table 4:** P-values and F-values obtained from response surface analysis for the response variable %R

Parameter	F value	P value
Model	72.07	0.0001<
A	103.9	0.0002
B	42.11	0.0013
C	389.41	0.0001<
AB	0.33	0.5929
AC	0.42	0.5464
BC	24.98	0.0041
A <sup>2</sup>	20	0.0066
B <sup>2</sup>	4.25	0.0942
C <sup>2</sup>	40.01	0.0015

**Table 5:** P-values and F-values obtained from response surface analysis for the response variable  $q_t$ .

Parameter	F value	P value
Model	56.50	<0.0001
A	16	0.0002
B	258.44	0.0102
C	153.39	<0.0001
AB	3.2	1.0001
AC	7.16	0.1339
BC	17.52	0.045
A <sup>2</sup>	0.4	0.0088
B <sup>2</sup>	4.64	1.0839
C <sup>2</sup>	15.99	0.0119

Based on the results, increasing the contact time between the adsorbent and the dye leads to an increase in the removal percentage. After 45 minutes, the trend stabilizes due to the saturation of available adsorption sites. Similarly, the increase in removal percentage with higher adsorbent dosage can be attributed to the greater number of active sites available for dye adsorption [21].

To evaluate the effect of enzymatic adsorbent dosage, various amounts of the organometallic enzyme-based adsorbent were tested at an initial dye concentration of 10 mg/L. The highest dye removal was observed with 5 g/L of adsorbent. Beyond this amount and after 45 minutes of contact time, the removal percentage remained constant (Figure 8).

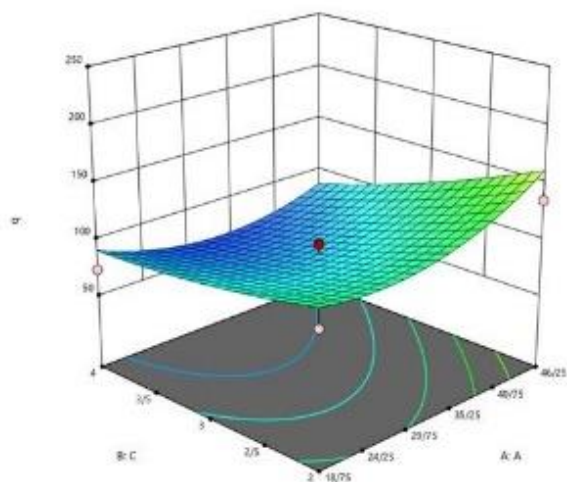


**Figure 8:** Response surface curve showing the effect of adsorbent dosage and contact time on adsorption capacity.

As the dye concentration in the solution increases, the removal percentage decreases. This reduction in adsorption efficiency can be attributed to the decreased ratio of available active sites on the adsorbent to the amount of dye present. As a result, a smaller fraction of the dye can be adsorbed onto the surface. The initial dye concentration is correlated with the amount of dye removed. The removal efficiency depends on the initial dye concentration, the number of enzyme active sites on the adsorbent surface, and the contact time. Although the total amount of dye removed may increase with higher dye concentrations, the removal percentage declines due to site saturation. Similarly, prolonged contact time enhances adsorption up to a point, but beyond this, increased dye concentration leads to a further decrease in removal efficiency [22-24].

### 3.3. Adsorption kinetics

The adsorption kinetics study was conducted to evaluate the effect of contact time and to determine parameters derived from kinetic models. The experimental data were analyzed using three kinetic models: pseudo-first-order, pseudo-second-order, and Elovich. The following equations (Eqs. 8 and 9) represent the pseudo-first-order model:

$$(dq/dt) = K_1(q_e - q_t) \quad (8)$$

$$\log(q_e - q_t) = \log(q_e) - (K_1/2.303) * t \quad (9)$$

In equation 9,  $q_t$  and  $q_e$  represent the adsorption capacities at time  $t$  and equilibrium, respectively, in mg/g.  $K_1$  is the rate constant of the pseudo-first-order model. The linear form of the pseudo-first-order kinetic equation is given by equation 9. The values of  $K_1$  and  $q_e$  can be determined from the slope and intercept of the linear plot of  $\log(q_e - q_t)$  versus  $t$  [25].

The pseudo-second-order kinetic model is represented by equations 10 and 11. In equation 10,  $K_2$  is the rate constant of the pseudo-second-order equation. The linear form is given in equation 11, where  $q_e$  and  $K_2$  can be calculated from the slope and intercept of the plot of  $t/q_t$  versus  $t$ .

$$(d(q)t/dt) = K_2 (q_e - q_t) \quad (10)$$

$$(t/q_t) = (1/K_2 q_e^2) + (1/q_e) * t \quad (11)$$

The Elovich model is represented by equations 12 and 13:

$$dq_t/dt = \alpha \exp(-bqt) \quad (12)$$

$$qt = \quad (13)$$

In equation 12,  $q_t$  is the amount of dye adsorbed at time  $t$  (mg/g),  $\alpha$  is the initial adsorption rate and reflects the rate of chemisorption at zero surface coverage, and  $b$  is the desorption constant, which is related to surface coverage and activation energy. equation 13 is the simplified linear form of the Elovich equation. The values of  $1/b \ln(\alpha\beta)$  and  $1/b$  correspond to the intercept and slope, respectively, of the plot of  $q_t$  versus  $\ln(t)$ .

### 3.4. Adsorption Isotherm

The adsorption isotherm was evaluated using the Freundlich and Langmuir models. The following equations describe the Freundlich and Langmuir isotherms. The Freundlich model is represented by equations 14 and 15:

$$\log q_e = \log k_f + (1/n) \log C_e \quad (14)$$

$$q_e = ((Q_m K_a C_e) / (1 + K_a C_e)) \quad (15)$$

In equation 14,  $K_f$  is the Freundlich constant, which relates to the binding energy of the adsorption process, and  $1/n$  is the heterogeneity factor, indicating the non-uniformity of the adsorbent surface. In equation 15,  $q_e$  represents the equilibrium adsorption capacity (mg/g),  $Q_m$  is the maximum adsorption capacity (mg/g),  $C_e$  is the equilibrium dye concentration (mg/L), and  $K_a$  is the adsorption equilibrium constant. The Langmuir model is expressed in Equation (16), where the intercept and slope of the plot of  $C_e/q_e$  versus  $C_e$  correspond to  $1/(K_a Q_m)$  and  $1/Q_m$ , respectively.

$$) \quad (16)$$

The results of the Elovich kinetic model for the adsorption of Diamine Green B dye onto the composite nanoadsorbent are presented in Figure 9. The pseudo-first-order kinetic model for the adsorption of Diamine Green B dye onto the composite nanoadsorbent is illustrated in Figure 10. The results of the pseudo-second-order kinetics for the adsorption of Diamine Green B dye onto the composite nanoadsorbent are shown in Figure 11.

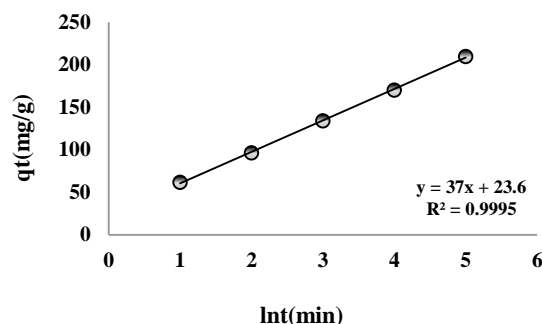


Figure 9: Elovich adsorption kinetics of Diamine Green B dye on the composite nanoadsorbent.

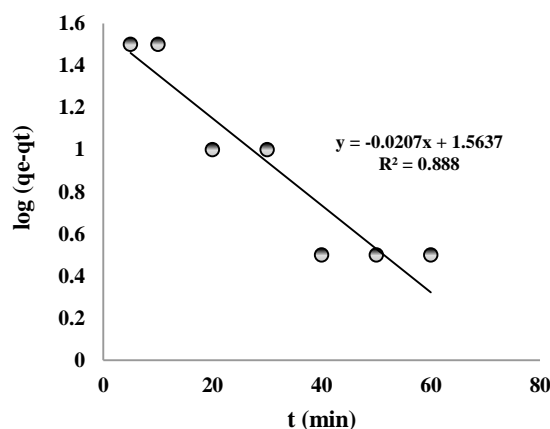


Figure 10: Pseudo-first-order kinetics for the adsorption of Diamine Green B dye on the composite nanoadsorbent.

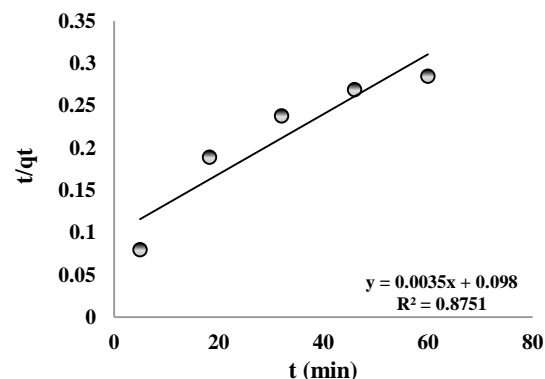


Figure 11: Pseudo-second-order kinetics for the adsorption of Diamine Green B dye on the composite nanoadsorbent.

The Freundlich adsorption isotherm for Diamine Green B dye on the composite nanoadsorbent is shown in Figure 12. The Langmuir adsorption isotherm for the adsorption of Diamine Green B dye on the composite nanoadsorbent is shown in Figure 13.

### 3.5. Adsorption thermodynamics

In the thermodynamic analysis of the adsorption process, three parameters must be determined: the standard enthalpy change  $\Delta H^\circ$ , the standard free energy change  $\Delta G^\circ$ , and the standard entropy change  $\Delta S^\circ$ . The values of  $\Delta H^\circ$  and  $\Delta S^\circ$  are obtained using equations 17 and 18. These parameters can be determined from the linear plot of  $\ln k$  versus  $T^{-1}$ , with the slope and width measured from the origin. The Gibbs free energy is calculated through equation 19.

$$\ln kd = \Delta S^\circ/R - \Delta H^\circ/RT \quad (17)$$

$$Kd = qe/Ce \quad (18)$$

$$\Delta G^\circ = -RT \ln kd \quad (19)$$

In these equations,  $R$  is the universal gas constant,  $T$  is the absolute temperature (in Kelvin), and  $K_d$  is the equilibrium constant, defined as the ratio of the amount of dye adsorbed on the organometallic adsorbent to the amount remaining in the solution [26].

The calculated thermodynamic parameters presented in Table 6 show that  $\Delta H^\circ$  has positive values, indicating that the adsorption process is endothermic. This finding is consistent with earlier results, which showed an increase in adsorption capacity with rising solution temperature. The positive values of  $\Delta H^\circ$  also suggest the formation of strong chemical interactions between the dye molecules and the adsorbent surface. As shown in Table 6, the other thermodynamic parameter,  $\Delta S^\circ$ , also has positive values, indicating a high affinity of the adsorbent for the dye and improved adsorption efficiency with increasing temperature in the solid-liquid phase. In contrast, the negative values of Gibbs free energy,  $\Delta G^\circ$ , confirm that the dye adsorption

process is spontaneous [27, 28].

The increase in negative  $\Delta G^\circ$  with rising temperature from 288 to 303 K may be attributed to the dehydration of both the dye molecules and the adsorbent surface, which enhances their interaction and makes adsorption more favorable at higher temperatures. The correlation coefficient ( $R^2$ ) was 0.978 at all three temperatures, indicating an excellent fit of

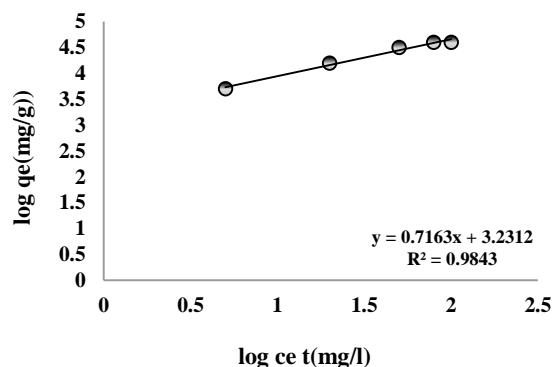


Figure 12: Freundlich adsorption isotherm for diamine green B dye on the composite nanoadsorbent.

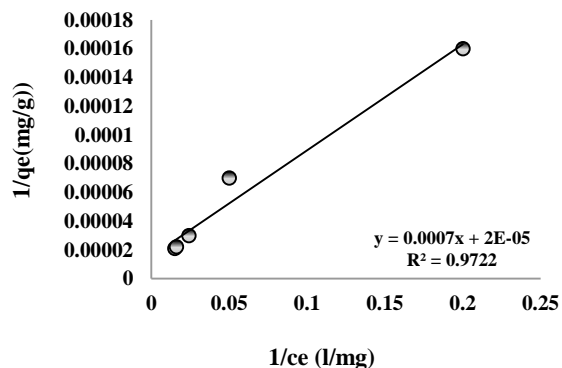


Figure 13: Langmuir adsorption isotherm of diamine green B dye on the composite nanoadsorbent.

Table 6: Thermodynamic variables of dye adsorption on enzyme-containing and enzyme-free organometallic adsorbents.

Sample	T (k)	$\Delta H$ (KJ/mol)	$\Delta S$ (J/mol K)	$\Delta G$ (KJ/mol)
LC @Fe-BTC	288	11.4	50	-2.918
	298			-3.418
	303			-3.668
Fe-BTC	288	5.2	22	-1.04
	298			-1.26
	303			-3.668

the thermodynamic model. Additionally, an increase in  $\ln K_d$  values with temperature was observed, further supporting the temperature-dependent nature of the adsorption process. The increase in dye removal with higher adsorbent dosage is attributed to the expansion of surface area, providing greater access to both adsorption and enzymatic degradation sites. As the active surface area of the catalyst increases, the bleaching capacity also improves. This effect arises from the combined contribution of adsorption and enzymatic decomposition in the initial phase. Eventually, as the available sites become saturated, the system reaches a stable number of active sites, resulting in a plateau in both adsorption efficiency and removal capacity. As the adsorbent dosage continues to increase (at a constant dye concentration), excess active sites remain unoccupied, resulting in no further improvement in the removal percentage. Consequently, the equilibrium adsorption capacity ( $q_e$ ) decreases. The results of this study are consistent with those reported by Mousavi et al. [14], who investigated the removal of Azo Orange 7 dye using a single-layer carbon nanotube adsorbent, as well as with the findings of Sheshmani et al. [19], who studied dye removal using chitosan-based adsorbents. In the present study, an increase in contact time resulted in higher dye adsorption efficiency, which can be attributed to an increased number of collisions and a greater probability of interaction between the dye molecules and the adsorbent surface. These findings align with those of Hamzeh et al. for the removal of Azo Orange 7 dye and

with the work of Greluk et al. [13] on the removal of Reactive Black 5 (RB5) dye. There is a strong correlation between the amount of dye removed and its initial concentration. The impact of initial dye concentration on removal efficiency is directly related to the number of enzyme active sites available on the adsorbent surface. As dye concentration increases, the percentage of dye removal decreases. This reduction is attributed to the limited number of available adsorption sites, which become insufficient at higher concentrations, thereby lowering enzymatic activity and overall adsorption efficiency. Consequently, the increased dye load leads to site saturation, resulting in diminished process performance [25-29].

#### 4. Conclusion

The results of this study demonstrate that the bio-modified metal-organic nanostructure is an effective adsorbent for dye removal, owing to its high surface area and enzymatic activity. Dye adsorption onto this material occurs with high adsorption capacity and energy. Kinetic studies reveal that the adsorption process closely follows the Elovich model, while the isotherm data show a strong correlation with the Freundlich model. Furthermore, the thermodynamic parameters indicate that the adsorption of the tested dye onto the enzymatic organometallic adsorbent is spontaneous, endothermic, and accompanied by an increase in system disorder.

#### 5. References

1. Alizadeh R, Tahmasebi F. Metal Organic Framework Nanocomposite Adsorbents with Enzyme Function to Remove Direct Green 6 Dye Pollution. *J Stud Colorworld*. 2024;14(1):45-55. <https://dor.isc.ac/dor/20.1001.1.22517278.1402.14.1.4.9>.
2. Mane VS, Mall ID, Srivastava VC. Use of bagasse fly ash as an adsorbent for the removal of brilliant. *Dyes Pigm*. 2007;73(3):269-78. <https://doi.org/10.1016/j.dyepig.2005.12.006>.
3. Donia AM, Atia AA, Al-amrani WA, El-Nahas AM. Effect of structural properties of acid dyes on their adsorption behaviour from aqueous solutions by amine modified silica. *J Hazard Mater*. 2019; 161(2):1544-1550. <https://doi.org/10.1016/j.jhazmat.2008.05.042>.
4. Asouhidou D, Triantafyllidis KS, Lazaridis NK, Matis KA. Adsorption of remazol red 3bs from aqueous solutions using APTES- and cyclodextrin-modified HMS-type mesoporous silicas. *Colloids Surf A Physicochem Eng Asp*. 2009;346(1):83-90. <https://doi.org/10.1016/j.colsurfa.2009.05.029>.
5. Taguchi A, Schüth F. Ordered mesoporous materials in catalysis. *Micropor Mesopor Mater*. 2014;77(1):1-45. <https://doi.org/10.1016/j.micromeso.2004.06.030>.
6. Xiao X, Zhang F, Feng Z, Deng S, Wang Y. Adsorptive removal and kinetics of methylene blue from aqueous solution using NiO/MCM-41 composite. *Physica E Low Dimens Syst Nanostruct*. 2015;6(5):4-12. <https://doi.org/10.1016/j.physe.2014.08.006>.
7. Michniewicz A, Ledakowicz S, Ullrich R, Hofrichter M. Kinetics of the enzymatic decolorization of textile dyes by laccase from *Cerrena unicolor*. *Dyes Pigm*. 2008;77(2): 295-302. <https://doi.org/10.1016/j.dyepig.2007.05.015>.
8. Sanchez M, de Asua I, Ruano D, Diaz K. Direct synthesis, structural features, and enhanced catalytic activity of the Basolite F300-like semi amorphous Fe-

- BTC framework. *Cryst Growth Des.* 2015;15:4498. <https://doi.org/10.1021/acs.cgd.5b00755>.
9. Castañeda Ramírez AA, García Rojas E, Medina RL, Contreras Larios JL, Suárez Parra R, Maubert Franco AM. Selective adsorption of aqueous diclofenac sodium, naproxen sodium, and ibuprofen using a stable Fe<sub>3</sub>O<sub>4</sub>-FeBTC metal-organic framework. *Materials.* 2021; 14:2293. <https://doi.org/10.3390/ma14092293>.
  10. Hou H, Zhou R, Wu P, Wu L. Removal of Congo red dye from aqueous solution with hydroxyapatite/ chitosan composite. *Chem Eng J.* 2012;211:336-342. <https://doi.org/10.1016/j.cej.2012.09.100>.
  11. Greluk M, Hubicki Z. Efficient removal of Acid Orange 7 dye from water using the strongly basic anion exchange resin Amberlite IRA-958. *Desalination.* 2011; 278(1):219-226. <https://doi.org/10.1016/j.desal.2011.05.024>.
  12. Shahbazi A, Younesi H, Badieli A. Synthesis of organic-inorganic hybrid amine based on nano-structured silicate materials and its application for removal of heavy metal ions from aqueous solution. *Water Wastewater.* 2013;23(84):13-21.
  13. Greluk M, Hubicki Z. Kinetics, isotherm and thermodynamic studies of reactive black 5 removal by acid acrylic resins. *Chem Eng J.* 2010;162(3):919-26. <https://doi.org/10.1016/j.cej.2010.06.043>.
  14. Moussavi SP, Emamjomeh MM, Ehrampoush MH, Behvari M, Jamshidi S. Removal of Acid Orange 7 dye from synthetic textile wastewater by single-walled carbon nanotubes: adsorption studies, isotherms and kinetics. *J Rafsanjan Univ Med Sci.* 2013;12(11):907-18. [Dor:20.1001.1.17353165.1392.12.11.4.8](https://doi.org/10.17353/165.1392.12.11.4.8).
  15. Paul M, Pal N, Bhaumik A. Selective adsorption and release of cationic organic dye molecules on mesoporous borosilicates. *Mater Sci Eng C.* 2012;32 (6): 1461-8. <https://doi.org/10.1016/j.msec.2012.04.026>.
  16. Bao C, Qu J, Zhou X, Xiang X, Zheng C, Zhang H, Zhou X. Adsorption behavior of Azo Dye CI Acid Red 14 in aqueous solution on surface soils. *J Environ Sci.* 2018; 20(6):704-9. [https://doi.org/10.1016/S1001-0742\(08\)62116-6](https://doi.org/10.1016/S1001-0742(08)62116-6).
  17. Chen Z, Zhou L, Zhang F, Yu C, Wei Z. Multi-carboxylic hyperbranched polyglycerol modified SBA-15 for the adsorption of cationic dyes and copper ions from aqueous media. *Appl Surf Sci.* 2012; 258 (13): 5291-8. <https://doi.org/10.1016/j.apsusc.2012.02.021>.
  18. Chen Z, Zhou L, Zhang F, Yu C, Wei Z. Multi-carboxylic hyper branched polyglycerol modified SBA-15 for the adsorption of cationic dyes and copper ions from aqueous media. *Appl Surf Sci.* 2012;258 (13): 5291-8. <https://doi.org/10.1016/j.apsusc.2012.02.021>.
  19. Sheshmani S, Ashori A, Hasanzadeh S. Removal of Acid Orange 7 from aqueous solution using magnetic graphene/chitosan: a promising nano-adsorbent. *Int J Biol Macromol.* 2014;68:218-24. <https://doi.org/10.1016/j.ijbiomac.2014.04.057>.
  20. Daneshvar N, Rasoulifard MH, Khataee AR, Hosseinzadeh F. Removal of CI Acid Orange 7 from aqueous solution by UV irradiation in the presence of ZnO nanopowder. *J Hazard Mater.* 2007;143(1-2):95-101. <https://doi.org/10.1016/j.jhazmat.2006.08.072>.
  21. Yanjing Y, Bai Y, Fengqi Z, Erbang Y, Jianhua Y, Chunlei X, et al. Effects of metal organic framework Fe-BTC on the thermal decomposition of ammonium perchlorate. *RSC Adv.* 2016;6(71):67308-14. <https://doi.org/10.1039/C6RA12634K>.
  22. Hosseini Z, Amirhandeh S, Salem A, Salem Sh. Adsorption of chromium iii species from colorant tannery wastewater by silica nano-particles. *J Stud Color World.* 2023;13(3):237-52. <https://doi.org/10.1001/1.22517278.1402.13.3.1.7> [In Persian]
  23. Navai Diva T. Various adsorbents for removal of rhodamine B dye: A review. *J Stud Color World.* 2023;12(4):387-404. <https://doi.org/10.1001/1.22517278.1401.12.4.6.7> [In Persian].
  24. Tabaraki R, Sadeghinejad N, Poorajam H. Study of dyes removal from binary system by hazelnut husk as agricultural waste by Response surface methodology. *J Stud Color World.* 2020;14:13-23. <https://doi.org/10.1001/1.17358779.1399.14.1.2.0> [In Persian]
  25. Haque FZ, Nandanwar R, Singh P. *Optik.* 2016; 128:191. <https://doi.org/10.1016/j.ijleo.2016.10.025>.
  26. Ren S, et al. Recent progress and future prospects of laccase immobilization on MOF supports for industrial applications. *Appl Biochem Biotechnol.* 2023;196(3):1-16. <https://doi.org/10.1007/s12010-023-0467-6>.
  27. Feng Y, et al. Recent advances in enzyme immobilization based on novel porous framework materials and its applications in biosensing. *Coord Chem Rev.* 2022;459:214414. <https://doi.org/10.1016/j.ccr.2022.214414>.
  28. Férey G, Mellot-Draznieks C, Serre C, Millange F. Crystallized frameworks with giant pores: Are there limits to the possible? *Acc Chem Res.* 2005; 38(4):217-25. <https://doi.org/10.1021/ar040163i>.
  29. Zhu L, Liu XQ, Jiang HL, Sun LB. Metal-organic frameworks for heterogeneous basic catalysis. *Chem Rev.* 2017;117(12):8129-8176. <https://doi.org/10.1021/acs.chemrev.7b00091>.

## How to cite this article:

Tahmasebi F, Alizadeh R, Samadi N. Study of the Kinetics, Thermodynamics, and Adsorption Isotherm of Diamine Green B dye using the Biocatalyst Laccase@Fe-BTC. *Prog Color Colorants Coat.* 2026;19(4):507-517. <https://doi.org/10.30509/pccc.2025.167477.1366>

